RADIATIVE COOLING

Subambient daytime radiative cooling of vertical surfaces

Fei Xie[1,2]†, Weiliang Jin[3,4]†, J. Ryan Nolen[5]†, Hao Pan[1,2]†, Naiqin Yi[1,2], Yang An[1], Zhiyu Zhang[6], Xiangtong Kong[1,2], Fei Zhu[1,2], Ke Jiang[7], Sicong Tian[7], Tianji Liu[1,2], Xiaojuan Sun[7], Longnan Li[1,2], Dabing Li[7], Yun-Feng Xiao[8], Andrea Alu[5,9]*, Shanhui Fan[3]*, Wei Li[1,2]*

Subambient daytime radiative cooling enables temperatures to passively reach below ambient temperature, even under direct sunlight, by emitting thermal radiation toward outer space. This technology holds promise for numerous exciting applications. However, previous demonstrations of subambient daytime radiative cooling require surfaces that directly face the sky, and these cannot be applied to vertical surfaces that are ubiquitous in real-world scenarios such as buildings and vehicles. Here, we demonstrate subambient daytime radiative cooling of vertical surfaces under peak sunlight using a hierarchically designed, angularly asymmetric, spectrally selective thermal emitter. Under peak sunlight of about 920 watts per square meter, our emitter reaches a temperature that is about 2.5°C below ambient temperature, corresponding to a temperature reduction of about 4.3° and 8.9°C compared with a silica-polymer hybrid radiative cooler and commercial white paint, respectively.

With global warming and rising peak daytime temperatures, the demand for cooling has been soaring (*1*). However, most conventional cooling strategies require energy input, which further increases greenhouse gas emissions and global warming (*2*). Enabling passive cooling strategies that do not require energy consumption is of great importance to address rising cooling demands and result in energy savings (*3*). Radiative cooling is a process that can dissipate heat in the form of thermal radiation into outer space through the atmospheric transparency window, offering an interesting passive cooling strategy (*4–8*). In its development, an important milestone was the demonstration of subambient daytime radiative cooling (*9*, *10*), which was realized through a nanophotonic structure engineered to strongly reflect sunlight while emitting infrared (IR) thermal radiation. Such a device can reach a temperature below the surrounding ambient temperature even when directly illuminated by peak sunlight and does not require energy input. Achieving subambient radiative cooling opens up a wide range of exciting applications in the context of cooling of buildings (*11–13*), vehicles (*14*), textiles (*15–18*), and water and energy harvesting (*19–23*), for which reaching subambient temperature is either essential or highly beneficial. To date, subambient daytime radiative coolers have been demonstrated in a variety of systems including nanophotonic structures (*9*, *10*), hybrid metamaterials (*24*), porous and nanofiber materials (*25–29*), and polymer films (*30*).

Most previous reports of daytime radiative cooling consider a surface that directly faces the sky and is typically implemented on a rooftop. This geometry facilitates the IR thermal emission toward the outer space, which is at the core of this approach to cooling. However, in many scenarios that require cooling, such as buildings, vehicles, and textiles, most exterior surfaces are in fact vertical (fig. S1) and thus do not directly face outer space, making it difficult to efficiently cool through IR thermal emission. Despite several efforts to do so (*31–33*), demonstrating subambient daytime radiative cooling for a vertical surface has been challenging. To understand the challenge of such a demonstration, we consider the net cooling power $P_{\mathrm{net}}(T)$ of a vertical surface (Fig. 1A):

$$P_{\mathrm{net}}(T) = P_{\mathrm{rad}}(T) - P_{\mathrm{Sun}} - P_{\mathrm{atm}}(T_{\mathrm{amb}}) - P_{\mathrm{ground}}(T_{\mathrm{g}}) - P_{\mathrm{cond+conv}}$$

Based on $P_{\mathrm{net}}(T)$, the surface thermally emits $P_{\mathrm{rad}}(T)$ and absorbs solar power P_{Sun}, downward atmospheric thermal radiation $P_{\mathrm{atm}}(T_{\mathrm{amb}})$, upward ground thermal radiation $P_{\mathrm{ground}}(T_{\mathrm{g}})$, and the convection and conduction thermal power $P_{\mathrm{cond+conv}}$ from the surrounding environment [see the supplementary text, section 1, in (*34*)] (fig. S2). We stress that the term $P_{\mathrm{ground}}(T_{\mathrm{g}})$ is unique to a vertical surface and is usually not relevant in a rooftop-cooling scenario (*10*).

To achieve subambient daytime radiative cooling of a vertical surface, the emitter must satisfy a very stringent set of constraints, including a strong reflectivity in the solar wavelength range, as well as a strong angular and spectral selectivity in its thermal emissivity in the mid-IR wavelength range. Compared with a horizontal surface, a vertical surface has substantially reduced cooling power because of the far more limited sky access, which translates into a far more stringent requirement on solar reflectance. Our theoretical analysis and experimental results indicate that a vertical surface needs to limit P_{Sun} to <40 W m^{-2} to achieve subambient cooling [see the supplementary text, section 2, in (*34*)] (figs. S3 to S5). In addition, a vertical surface is subject to upward ground radiation. In the daytime, the ground temperature T_{g} can be much higher than the ambient temperature T_{amb} due to solar heating (fig. S6) (*35*). As a result, conventional thermal emitters optimized for deployment on a horizontal surface, which are typically omnidirectional, cannot reach subambient temperature when placed on a vertical surface assuming peak daytime sunlight conditions [see the supplementary text, section 3, in (*34*)] (figs. S7 to S9). Rather, the emitter needs to support a strong angularly asymmetric thermal emission to minimize the absorption from the upward ground radiation $P_{\mathrm{ground}}(T_{\mathrm{g}})$ and at the same time maximize emission toward the sky. Finally, the emissivity also needs to be spectrally selective in the atmospheric transparency window (i.e., 8 to 13 μm) to minimize the absorption of downward atmospheric thermal radiation $P_{\mathrm{atm}}(T_{\mathrm{amb}})$ and solar absorption P_{Sun}.

The above constraints pose challenges in realizing subambient daytime radiative cooling of vertical surfaces. Over the past decades, engineered structures have allowed thermal radiation to be tailored (*36*, *37*), with demonstrations of both spectral and angular control of thermal emission (*9*, *10*, *24*, *27*, *31–33*, *38–43*) (see fig. S10 for an overview). However, these emitters do not meet the angular and spectral requirements to achieve subambient daytime radiative cooling of vertical surfaces.

We have proposed, designed, and demonstrated an angularly asymmetric, spectrally selective (AS) thermal emitter for achieving subambient daytime radiative cooling of vertical surfaces under peak sunlight. Our emitter consists of a sawtooth grating with periodicity substantially larger than the thermal wavelength, covered by an ultraviolet-visible (UV-VIS) reflective IR transparent nanoporous polyethylene (nanoPE) film. Under a peak solar

[1]GPL Photonics Laboratory, Key Laboratory of Luminescence Science and Technology, Chinese Academy of Sciences & State Key Laboratory of Luminescence and Applications, Changchun Institute of Optics, Fine Mechanics and Physics, Chinese Academy of Sciences, Changchun, 130033, China. [2]University of Chinese Academy of Sciences, Beijing 100039, China. [3]Department of Electrical Engineering, Ginzton Laboratory, Stanford University, Stanford, CA 94305, USA. [4]Flexcompute Inc., Belmont, MA 02478, USA. [5]Photonics Initiative, Advanced Science Research Center, City University of New York, New York, NY 10031, USA. [6]Changchun Institute of Optics, Fine Mechanics and Physics, Chinese Academy of Sciences, Changchun 130033, China. [7]Key Laboratory of Luminescence Science and Technology, Chinese Academy of Sciences & State Key Laboratory of Luminescence and Applications, Changchun Institute of Optics, Fine Mechanics and Physics, Chinese Academy of Sciences, Changchun, 130033, China. [8]State Key Laboratory for Mesoscopic Physics and Frontiers Science Center for Nano-optoelectronics, School of Physics, Peking University, Beijing 100871, China. [9]Physics Program, Graduate Center, City University of New York, New York, NY 10016, USA.
***Corresponding author. Email: weili1@ciomp.ac.cn (W.L.); shanhui@stanford.edu (S.F.); aalu@gc.cuny.edu (A.A.)**
†These authors contributed equally to this work.

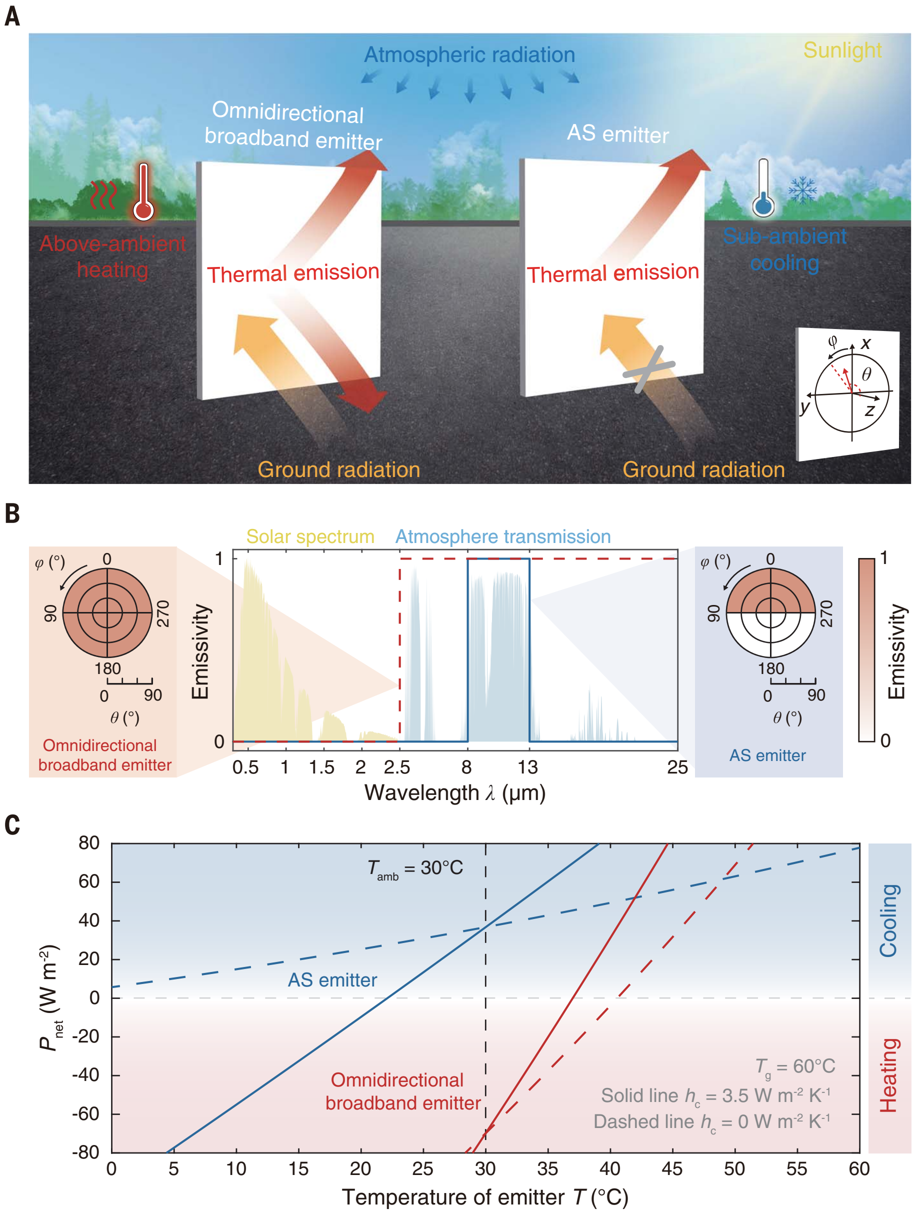

Fig. 1. Design considerations for subambient daytime radiative cooling of vertical surfaces. (**A**) In the daytime, a vertically oriented, omnidirectional broadband thermal emitter fails to cool because of the absorption of ground radiation and reduced sky access. By contrast, we tailored both the angular and spectral properties of our emitter to minimize the absorption of upward ground radiation, downward atmospheric thermal radiation and sunlight. (**B**) Angular and spectral emissivity of an omnidirectional broadband thermal emitter (with zero absorption in the solar spectrum) and of an AS thermal emitter (with selective emission from 8 to 13 μm and zero solar absorption). The θ (zenith) and ϕ (azimuth) angles in (A) and (B) define the direction of thermal emission. (**C**) Net cooling power P_{net} as a function of emitter temperature T for the omnidirectional broadband thermal emitter and the AS emitter when vertically oriented. In thermal equilibrium, where $P_{net}(T) = 0$, the AS emitter (blue solid line) achieves ~7.9°C subambient cooling and a temperature reduction of 14.9°C compared with the omnidirectional broadband thermal emitter (red solid line) under a typical summer daytime condition with appropriate thermal insulation (h_c = 3.5 W m^{-2} K^{-1}) (7, 44). With perfect thermal insulation (h_c = 0 W m^{-2} K^{-1}), the AS emitter (blue dashed line) can reach a temperature of >40°C lower than the omnidirectional broadband thermal emitter (red dashed line). We assumed an ambient temperature T_{amb} of 30°C and a ground temperature T_g of 60°C in summer daytime (fig. S6) (35).

irradiance of over 920 W m^{-2}, our emitter reaches a temperature of 2.5° ± 0.7°C below the ambient temperature, as well as a temperature reduction of 4.3° ± 0.2°C and 8.9° ± 0.2°C compared with the silica-polymer hybrid radiative cooler with a state-of-the-art performance and commercial white paint, respectively. Our results achieve angular and spectral control of thermal radiation and demonstrate subambient daytime radiative cooling of vertical surfaces even under peak sunlight. This demonstration suggests untapped opportunities in radiative cooling and point toward new directions in manipulating radiative heat flow.

Analysis and design of the AS thermal emitter

We showcase the full potential of an ideal AS thermal emitter and compare it with an omnidirectional broadband thermal emitter. We assume that both of them have ideal zero absorption in the solar spectrum. In the mid-IR wavelength range, the AS thermal emitter has unity and zero emissivity for the top and bottom halves of the hemispherical space, respectively, with spectrally selective emission from 8 to 13 μm (Fig. 1B). When vertically oriented, an AS thermal emitter can theoretically achieve a 7.9°C subambient cooling and a temperature reduction of 14.9°C compared with an omnidirectional broadband thermal emitter (Fig. 1C) under typical daytime conditions with appropriate thermal insulation (h_c = 3.5 W m^{-2} K^{-1}) (7, 44). By contrast, even with complete suppression of solar absorption, the omnidirectional broadband thermal emitter cannot reach subambient temperature when deployed on a vertical surface because of the absorption of ground radiation.

Our thermal emitter design consists of a sawtooth grating covered by a nanoPE film (Fig. 2A). The sawtooth grating is made of a horizontal and a slanted surface (the description of the surfaces refers to the case where the emitter is deployed vertically). The slanted surface is covered by two layers of silver (Ag) sandwiching a layer of silicon nitride (SiN). The horizontal surface is covered by one layer of Ag with another layer of SiN on top. In this design, the Ag layers provide strong reflection in the VIS and near-IR range (Fig. 2B). Because the Ag layers are absorptive in the UV wavelength range, we used nanoPE film, which has air pores of different sizes ranging from 0.3 to 1 μm, supporting multiple Mie resonances (45) (Fig. 2C), to strongly reflect solar irradiation in the UV and VIS wavelength range. The combination of the Ag layers and the nanoPE film thus results in strong reflection over the entire solar wavelength range, satisfying the solar reflectivity requirement.

The spectrally selective thermal emission of our structure arises primarily from the SiN layer. SiN is chosen for its low loss across the entire solar wavelength range and for its phonon polariton resonance around 11 μm (fig. S11). We chose an optimized thickness of 4 μm for the SiN layer to enable spectrally selective thermal emission in the 8- to 13-μm range. The SiN layer is separated from the sawtooth grating by an Ag layer on both the horizontal and the slanted surfaces, ensuring that the emission

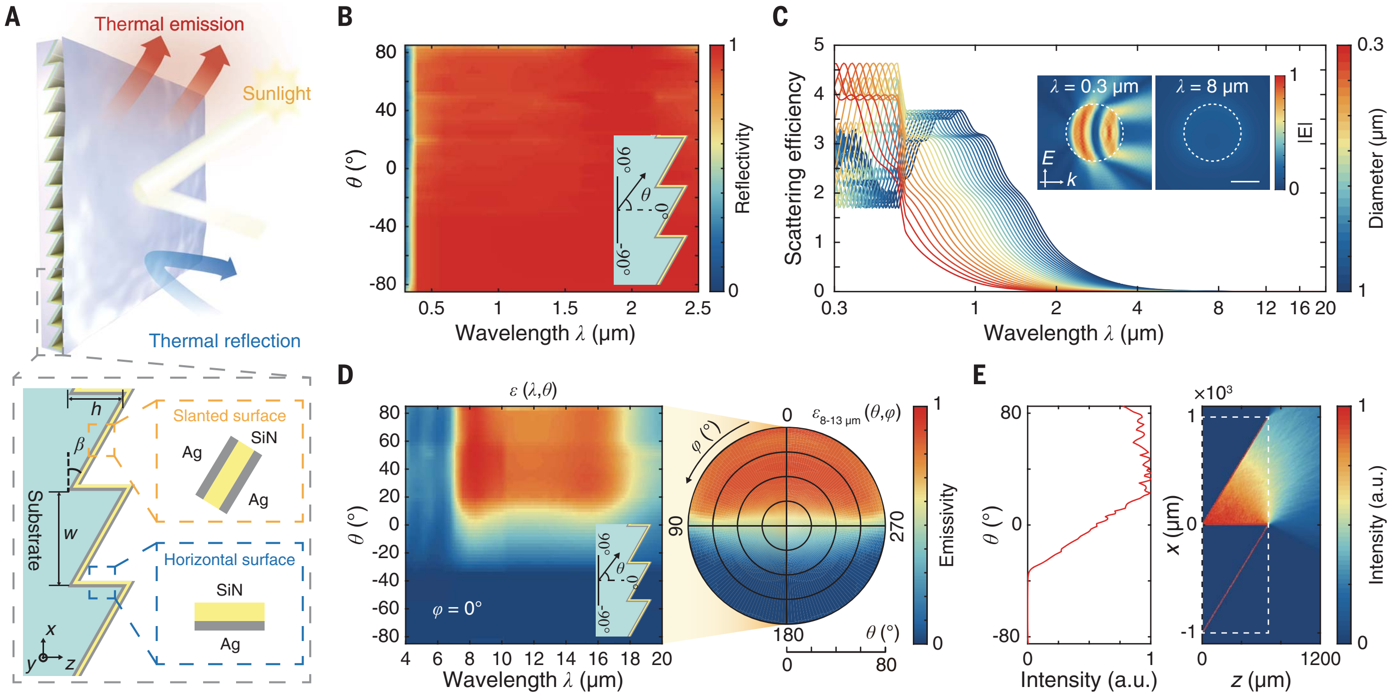

Fig. 2. Design of the AS emitter. (**A**) Schematic of the AS emitter consisting of a sawtooth grating covered by a UV-VIS–reflective, IR-transparent nanoPE film. The sawtooth grating (with period *w*, height *h*, and tilt angle β) is covered by two heterostructures, Ag–SiN–Ag and Ag–SiN on the slanted and horizontal surfaces, respectively, to enable both angularly asymmetric and spectrally selective emission. (**B**) Simulated spectral solar reflection of our designed sawtooth grating under different incident angles. (**C**) Scattering efficiency of air pores in polyethylene with different diameters over the wavelength range of 0.3 to 20 μm. Air pore size between 0.3 and 1 μm is optimal for simultaneous strong UV-VIS scattering and negligible mid-IR scattering. Insets show the calculated scattering fields of a 1-μm air pore at the wavelength of 0.3 and 8 μm, respectively. Scale bar, 0.5 μm. *E*, electric field of the incident light; *k*, wave vector of the incident light. (**D**) Spectral angular emissivity $\varepsilon(\lambda,\theta)$ (left) and 8- to 13-μm averaged emissivity $\varepsilon_{8-13\mu m}(\theta,\phi)$ (right) varying with zenith (θ) and azimuth (ϕ) angles. (**E**) Angular (left) and spatial (right) distribution of thermal radiation intensity from sawtooth grating at the wavelength of 11 μm calculated using the fluctuation-dissipation theorem. For visualization purposes, we only show the emission field from one unit cell. The structural parameters are w = 1000 μm, h/w = 2/3, d_{Ag} = 0.15 μm, and d_{SiN} = 4 μm.

comes only from the SiN layer, not from the grating substrate.

The angularly asymmetric emission stems from the sawtooth grating with broken in-plane mirror symmetry (*42*). On the slanted surfaces, the outermost Ag layer ensures that downward emission to the ground is suppressed. The upward emission to the sky has a primary contribution from the SiN layer on the horizontal surfaces. The grating period *w* must be larger than the wavelength to enable angular-asymmetric emission because of the constraints stemming from thermodynamics and reciprocity (*46*, *47*) (fig. S12), as well as to support a quasicontinuous frequency coverage of light coupling (*48*) [see the supplementary text, section 4, in (*34*)] (fig. S13). In addition, the angular coverage of thermal emission can be easily tuned by changing the aspect ratio h/w (or, equivalently, the tilt angle β) of the sawtooth grating (fig. S14), a useful feature for designing radiative coolers of inclined surfaces with different orientations (fig. S5A).

The sawtooth grating exhibits spectrally selective and angularly asymmetric emissivity (Fig. 2D). We can visualize these angularly asymmetric features with a direct calculation of thermal emission based on the fluctuation-dissipation theorem (Fig. 2E) (*34*). The tailored nanoPE film's pores size enables a negligible scattering efficiency in the mid-IR range to ensure the high mid-IR transmission and AS features of our designed emitter.

The angularly asymmetric response of a sawtooth grating has been described in the literature (*42*, *49*, *50*), and very recently there has been a report of radiative cooling of a vertical surface using an angularly selective emitter made of periodically placed tilted wedges partially coated with aluminum (*32*). However, that study (*32*) did not report subambient cooling. Our design achieves simultaneous angular and spectral selectivities, which is essential to reaching subambient temperatures for daytime radiative cooling of a vertical surface.

Fabrication and characterization

We experimentally realized the optimized sawtooth grating using a template molding technique for scalable manufacturing, followed by a standard thin film–coating process (fig. S15) (*34*). The solar reflectivity of the sawtooth grating can be enhanced by covering a nanoPE film (Fig. 3A and fig. S16). The combined structure formed by the sawtooth grating and nanoPE film shows an omnidirectional reflectivity of 0.978 averaged over the solar spectrum (Fig. 3B). In the mid-IR wavelength range, the nanoPE film provides not only high total transmittance (T_{total}) but also high direct transmittance (T_{direct}) (Fig. 3C), since the pores in the film are deeply subwavelength. The IR properties of the sawtooth grating (Fig. 3D) were characterized using a customized angle-resolved thermal emission spectrum measurement (ATESM) system (Fig. 3E and fig. S17). We observe a clear angularly asymmetric, spectrally averaged emissivity $\varepsilon_{8-13\mu m}(\theta,\phi)$, with strong emissivity only in the top half of the hemispherical space (Fig. 3D, right) and spectral-selectivity from 8 to 13 μm with angularly asymmetric feature (Fig. 3D, left), showing reasonable agreement with theoretical predictions (Fig. 2D). Therefore, the combination of the sawtooth grating and the nanoPE film with high IR transmittance results in the creation of an AS thermal emitter (fig. S18). We can further visualize this through

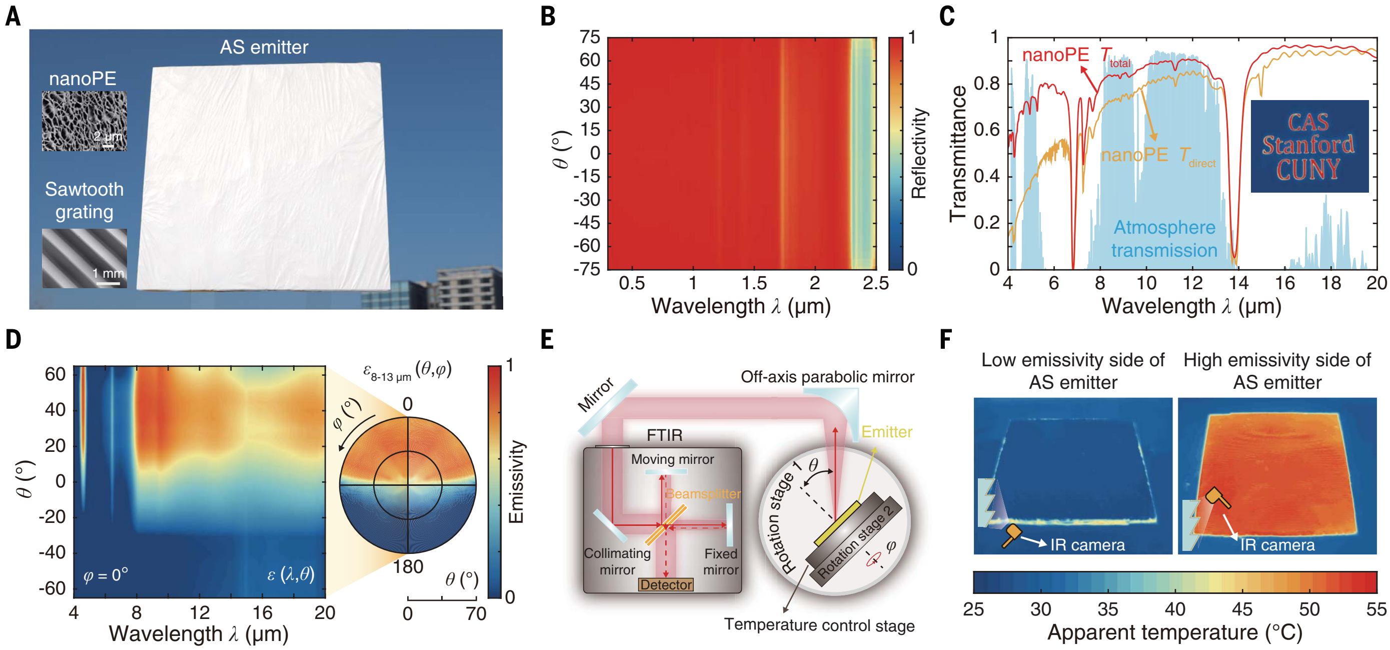

Fig. 3. Experimental characterization of the AS emitter. (**A**) Photograph of the 35 × 35 cm AS emitter. Insets show scanning electron microscope images of the sawtooth grating and nanoPE film. (**B**) Measured solar reflectivity spectrum of the AS emitter under different incident angles. The AS emitter shows an omnidirectional solar reflectivity of 0.978. (**C**) The nanoPE film has strong direct (T_{direct}) (yellow line) and total (T_{total}) (red line) IR transmittance to preserve the angularly asymmetric emission features. Its excellent direct IR transmission can be visualized through an IR pattern covered by this nanoPE film (see thermography image in the inset). (**D**) Left: angle-resolved thermal emission spectrum measurements (ATESM) revealing the sawtooth grating's spectral selectivity from 8 to 13 μm and angularly asymmetric features. Right: the angular emissivity distribution showing a clear angularly asymmetric averaged emissivity $\varepsilon_{8-13\mu m}(\theta,\phi)$ over the top half of the hemispherical space. (**E**) Schematic of the customized ATESM setup. (**F**) Thermography images of the AS emitter taken from opposing directions showing a clear contrast in output radiation or apparent temperature.

an IR camera, highlighting that a clear contrast in the output radiation or apparent temperature from opposing sides of the AS thermal emitter can be observed (Fig. 3F).

Demonstration of directional and subambient daytime radiative cooling

To demonstrate the efficacy of our approach to radiative cooling, we consider two scenarios. The first is implemented in vacuum to minimize heat convection and conduction to highlight the effect of directional radiative cooling. We used a customized vacuum chamber radiative cooling setup (*34*) with its inner surface maintained at −13°C as a cold background through a feedback control. Inside the chamber, a heater (1.2 by 0.75 m) is placed on the ground. Our AS thermal emitter (10 by 10 cm) and an omnidirectional broadband thermal emitter of the same size are placed vertically 40 cm above the edge of the heater (Fig. 4A), forming a view factor $F_{emitter\rightarrow heater}$ of 0.19. As we increase the heater temperature to 48.9°, 73.3°, and 96.9°C, the omnidirectional broadband thermal emitter is radiatively heated up by the ground radiation from the heater (Fig. 4B). By contrast, our AS thermal emitter is radiatively cooled by the cold background and shows temperature drops of 14.1°, 19.8°, and 25.6°C compared with the omnidirectional broadband thermal emitter, demonstrating effective directional radiative cooling.

Next, we demonstrate subambient daytime radiative cooling of our AS thermal emitter in realistic outdoor conditions (*34*). We performed the experiments with continuous outdoor temperature measurements on clear summer days in Beijing, China. For comparison, we used a silica-polymer hybrid radiative cooler and a commercial solar-reflective white paint as control groups. The silica-polymer hybrid radiative cooler was prepared by randomly mixing dielectric microspheres in a polymeric matrix with a state-of-the-art performance (solar reflectivity 0.97, IR emissivity >0.9; can achieve 6.5°C subambient daytime radiative cooling if horizontally placed, as shown in fig. S9). The chosen white paint is a typical benchmark considered in previous literature (*34*). Both control groups exhibit omnidirectional thermal emission features (fig. S19). We vertically mounted all three samples in the experimental setup shown in Fig. 4, C and D. To consider the most stringent conditions, we faced the setup to the south with the strongest solar irradiance. As shown in Fig. 4, E and F, over the entire day, the AS thermal emitter maintained a steady-state temperature substantially below the ambient temperature, 2.5° ± 0.7°C below the ambient temperature during 11:30 AM to 12:30 PM (local time), when the ambient temperature is in the range of 36° to 41°C, the ground temperature is in the range of 54° to 58°C, and the solar irradiance is in the range of 864 to 922 W m^{-2}. By contrast, the silica-polymer hybrid radiative cooler and commercial white paint fail to reach subambient temperature during the time periods 9:30 AM to 3:30 PM (local time) and 9:00 AM to 5:00 PM (local time), respectively, when peak cooling demand usually occurs. Therefore, under peak sunlight (11:30 AM to 12:30 PM, local time), the AS thermal emitter enables subambient radiative cooling with a temperature reduction of 4.3° ± 0.2°C and 8.9° ± 0.2°C compared with the silica-polymer hybrid radiative cooler and commercial white paint, respectively, both of which are at a temperature above ambient. We stress that in a less demanding scenario in which all samples face to the north with minimized direct solar irradiance on the vertical surface, the silica-polymer hybrid radiative cooler and commercial white paint still cannot reach subambient temperature (fig. S20), but our AS thermal emitter can, highlighting the role of ground radiation. To further explore the radiative cooling performance of emitters with

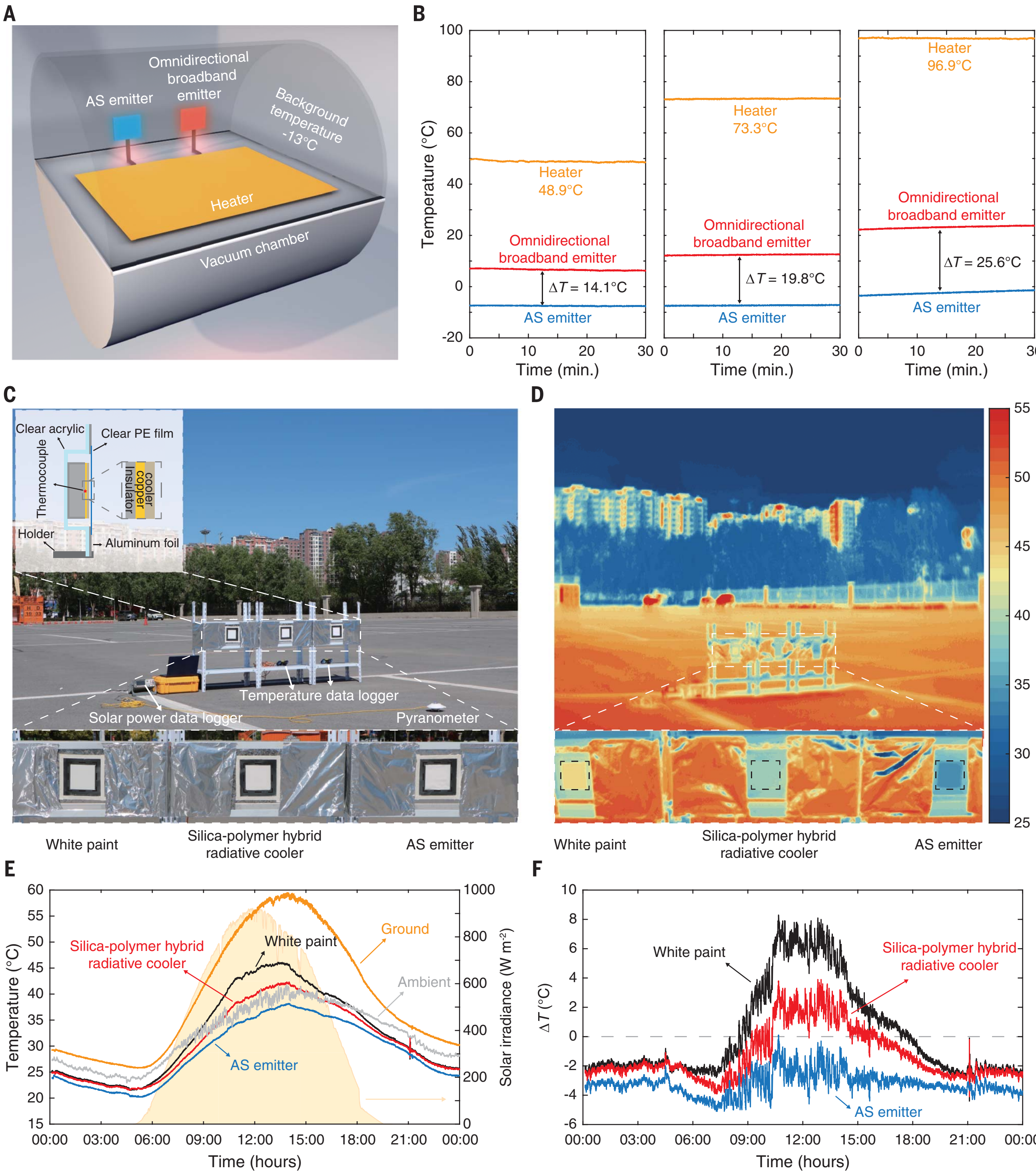

Fig. 4. Demonstration of angularly asymmetric directional radiative cooling. (**A**) Schematic of a customized vacuum chamber radiative cooling setup with an inner surface maintained at −13°C as a cold background and a heater placed on the ground. An AS thermal emitter and an omnidirectional broadband thermal emitter of the same size are placed vertically above the edge of the heater with a view factor $F_{emitter \rightarrow heater}$ of 0.19. (**B**) As the heater temperature (yellow line) increases to 48.9°, 73.3°, and 96.9°C, the omnidirectional broadband thermal emitter (red line) is radiatively heated up. By contrast, the AS thermal emitter (blue line) shows a temperature reduction of 14.1°, 19.8°, and 25.6°C compared with the omnidirectional broadband thermal emitter. (**C** and **D**) Photograph and thermography images of the outdoor daytime radiative cooling setup. Top insets in (C) show schematics of the setup. Bottom insets in (C) and (D) show a magnified view of the white paint, silica-polymer hybrid radiative cooler and the AS emitter. (**E** and **F**) Full-day solar irradiance, temperature data, and temperature difference from ambient. Under a peak solar irradiance of >920 W m^{-2} (during 11:30 AM to 12:30 PM, local time), only the AS emitter achieves subambient radiative cooling and shows a temperature of 2.5° ± 0.7°C below the ambient temperature, as well as a temperature reduction of 4.3° ± 0.2°C and 8.9° ± 0.2°C compared with the silica-polymer hybrid radiative cooler and commercial white paint, respectively.

different orientations (facing north, east, and west), we calculated the steady-state temperature of emitters over a full day [see the supplementary text, section 5, in (*34*)] (figs. S21 and S22), which highlights the wide applicability of our proposed approach.

Similar to many standard radiative cooling experiments, in our experiments, the cooling structure formed by the sawtooth grating and the nanoPE film is placed in an enclosure covered by a wind shield made of conventional uniform PE film. We also performed additional experiments by removing the PE film cover and using the designed nanoPE film itself as the wind shield (fig. S23). We observed similar subambient daytime radiative cooling performance, indicating the efficacy of nanoPE film for reducing convection. Therefore, such a hierarchically designed AS thermal emitter can be readily applied as an exterior cooling surface without additional complexity.

To further investigate the cooling performance of the AS thermal emitter in practical scenarios and to consider the most stringent conditions, we conducted additional outdoor experiments with all emitters aimed toward a south-facing wall that is the hottest at noon (Fig. 5A). To effectively reject the radiation from the ground and wall, we redesigned and fabricated an AS emitter with the tilt angle β of 11°. The AS emitter maintains a steady-state temperature below the ambient temperature during 11:00 AM to 1:00 PM (local time), when the ground temperature is in the range of 44° to 53°C, the wall temperature is in the range of 38° to 45°C, and the solar irradiance is in the range of 700 to 900 W m^{-2} (Fig. 5B). By contrast, the silica-polymer hybrid radiative cooler and solar reflective white paint failed to cool. The AS emitter showed a temperature reduction of 3.5° and 4.6°C compared with the silica-polymer hybrid radiative cooler and commercial white paint.

Building upon our experimental demonstration, we theoretically analyzed the ultimate

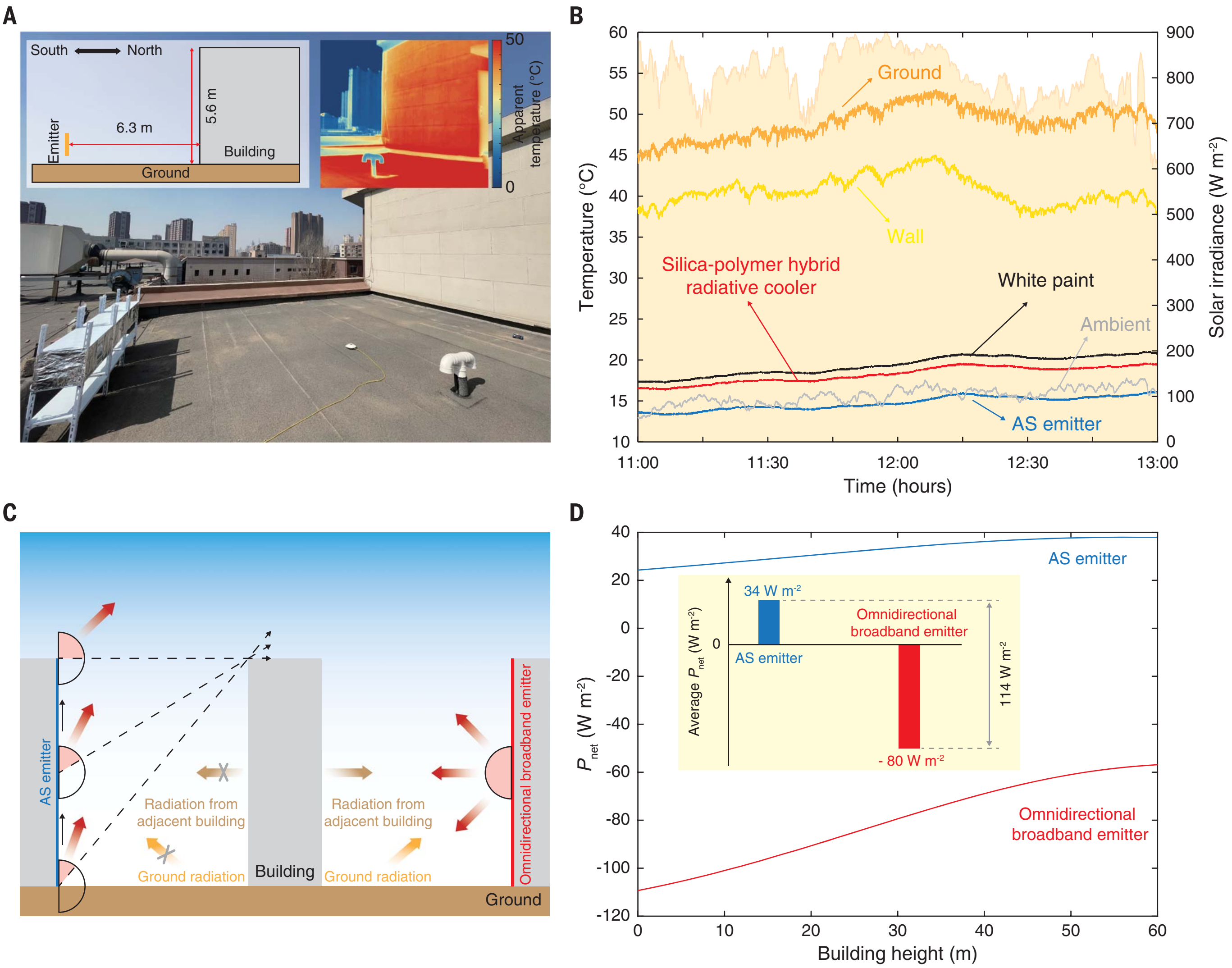

Fig. 5. Experimental and theoretical analysis for building wall applications. (**A**) Photograph and schematic of the outdoor setup facing the building wall. (**B**) Measured solar irradiance, temperature of all emitters, ambient temperature, ground temperature, and building wall temperature. During 11:00 AM to 1:00 PM (local time), only the AS emitter achieves subambient radiative cooling when facing the building wall. (**C**) Schematic of the impact of adjacent buildings on the gradient AS emitter and omnidirectional broadband emitter. (**D**) Net cooling power at different locations on a building wall covered with a gradient AS emitter or omnidirectional broadband emitter. The average cooling power of a gradient AS emitter is ~114 W m^{-2} higher than that of an omnidirectional broadband emitter. Here, we assume that the ambient temperature is 30°C, the ground temperature is 60°C, and the wall temperature is 50°C. We considered two buildings with the same height of 60 m and a spacing of 50 m between them.

theoretical cooling potential considering the interbuilding thermal radiation (Fig. 5C). To maximize the cooling power, an ideal building wall should have a gradient in its angular distribution of emissivity. The ideal gradient AS emitter can maintain a net cooling power covering the entire wall (Fig. 5D). The lower end wall was still able to maintain net cooling, even with a large view factor facing the hotter surroundings (~78% of the field of view). By contrast, the omnidirectional broadband emitter is heated by the ground and adjacent buildings and fails to cool. The average cooling power of a gradient AS emitter is ~114 W m^{-2} higher than that of an omnidirectional broadband emitter.

Conclusions

We developed a hierarchically designed AS thermal emitter that achieves daytime subambient radiative cooling from vertical surfaces. This emitter outperforms any flat emitters, which have a symmetric angular response due to the constraint of reciprocity and therefore will always absorb emission from the ground. The daytime subambient radiative cooling from vertical surfaces shown here enables passive cooling from two-dimensional horizontal surfaces to three-dimensional realistic settings (such as buildings, vehicles, and textiles) with a large expansion of effective cooling areas, opening up a different degree of freedom in radiative cooling. Leveraging the rapid advances in radiative cooling over the past decade (*7*, *8*), a plethora of previous research on photonic design (*9*, *10*), materials (*24*–*26*), scalable manufacturing techniques (*12*, *18*, *24*, *30*), and a wide range of applications (*15*, *19*, *21*, *51*, *52*) for radiative cooling may be expected to be readily deployed to explore this opportunity and enable emerging directions for radiative cooling. More broadly, the capability of AS thermal emission may challenge the current design methodology in existing radiative heat– and energy-transfer systems, with potential impacts of reduced heating and global energy consumption. Our results also point to fundamentally new opportunities in manipulating meaningful heat and information flow in which new, highly efficient cooling, heating, energy-transfer, and harvesting capabilities can emerge.

REFERENCES AND NOTES

1. International Renewable Energy Agency (IRENA), International Energy Agency (IEA), REN21, "Renewable energy policies in a time of transition: Heating and cooling" (IRENA, IEA, REN21, 2020); https://www.irena.org/publications/2020/Nov/Renewable-Energy-Policies-in-a-Time-of-Transition-Heating-and-Cooling.
2. IPCC, *Global Warming of 1.5°C* (Cambridge Univ. Press, 2022).
3. B. Grocholski, *Science* **370**, 776–777 (2020).
4. S. Catalanotti *et al*., *Sol. Energy* **17**, 83–89 (1975).
5. C. G. Granqvist, A. Hjortsberg, *J. Appl. Phys.* **52**, 4205–4220 (1981).
6. A. R. Gentle, G. B. Smith, *Nano Lett.* **10**, 373–379 (2010).
7. X. Yin, R. Yang, G. Tan, S. Fan, *Science* **370**, 786–791 (2020).
8. S. Fan, W. Li, *Nat. Photonics* **16**, 182–190 (2022).
9. E. Rephaeli, A. Raman, S. Fan, *Nano Lett.* **13**, 1457–1461 (2013).
10. A. P. Raman, M. A. Anoma, L. Zhu, E. Rephaeli, S. Fan, *Nature* **515**, 540–544 (2014).
11. E. A. Goldstein, A. P. Raman, S. Fan, *Nat. Energy* **2**, 17143 (2017).
12. S. Wang *et al*., *Science* **374**, 1501–1504 (2021)
13. K. Tang *et al*., *Science* **374**, 1504–1509 (2021).
14. S.-Y. Heo *et al*., *Sci. Adv.* **6**, eabb1906 (2020).
15. P.-C. Hsu *et al*., *Science* **353**, 1019–1023 (2016).
16. X. A. Zhang *et al*., *Science* **363**, 619–623 (2019).
17. B. Zhu *et al*., *Nat. Nanotechnol.* **16**, 1342–1348 (2021).
18. S. Zeng *et al*., *Science* **373**, 692–696 (2021).
19. I. Haechler *et al*., *Sci. Adv.* **7**, eabf3978 (2021).
20. M. Zhou *et al*., *Proc. Natl. Acad. Sci. U.S.A.* **118**, e2019292118 (2021).
21. A. P. Raman, W. Li, S. Fan, *Joule* **3**, 2679–2686 (2019).
22. Z. Chen, L. Zhu, W. Li, S. Fan, *Joule* **3**, 101–110 (2019).
23. L. Zhou *et al*., *Cell Rep. Phys. Sci.* **2**, 100338 (2021).
24. Y. Zhai *et al*., *Science* **355**, 1062–1066 (2017).
25. J. Mandal *et al*., *Science* **362**, 315–319 (2018).
26. T. Li *et al*., *Science* **364**, 760–763 (2019).
27. D. Li *et al*., *Nat. Nanotechnol.* **16**, 153–158 (2021).
28. X. Zhao *et al*., *Science* **382**, 684–691 (2023).
29. K. Lin *et al*., *Science* **382**, 691–697 (2023).
30. L. Zhou *et al*., *Nat. Sustain.* **2**, 718–724 (2019).
31. J. Mandal *et al*., *Cell Rep. Phys. Sci.* **5**, 102065 (2024).
32. J. Zhou *et al*., *Joule* **7**, 2830–2844 (2023).
33. R. Wu *et al*., *Science* **384**, 1203–1212 (2024).
34. Materials and methods are available as supplementary materials.
35. T. Clifton, T. W. Khoo, A. Andrawos, S. Thomson, J. E. Greenwood, *Burns* **42**, 453–456 (2016).
36. W. Li, S. Fan, *Opt. Express* **26**, 15995–16021 (2018).
37. D. G. Baranov *et al*., *Nat. Mater.* **18**, 920–930 (2019).
38. J. Xu, J. Mandal, A. P. Raman, *Science* **372**, 393–397 (2021).
39. J. Yu, R. Qin, Y. Ying, M. Qiu, Q. Li, *Adv. Mater.* **35**, e2302478 (2023).
40. J. R. Nolen, A. C. Overvig, M. Cotrufo, A. Alù, *Nat. Nanotechnol.* 10.1038/s41565-024-01763-6 (2024).
41. J.-J. Greffet *et al*., *Nature* **416**, 61–64 (2002).
42. L. Sun *et al*., *Nat. Photonics* **13**, 180–184 (2019).
43. A. C. Overvig, S. A. Mann, A. Alù, *Phys. Rev. X* **11**, 021050 (2021).
44. D. Zhao *et al*., *Joule* **3**, 111–123 (2019).
45. H. C. Hulst, *Light Scattering by Small Particles* (Courier Corporation, 1981).
46. W. C. Snyder, Z. Wan, X. Li, *Appl. Opt.* **37**, 3464–3470 (1998).
47. C. Guo, B. Zhao, S. Fan, *Phys. Rev. X* **12**, 021023 (2022).
48. Y. X. Yeng *et al*., *Proc. Natl. Acad. Sci. U.S.A.* **109**, 2280–2285 (2012).
49. X. Yin, J. Jin, M. Soljačić, C. Peng, B. Zhen, *Nature* **580**, 467–471 (2020).
50. Y. Chen *et al*., *Nature* **613**, 474–478 (2023).
51. L. Cai *et al*., *Adv. Mater.* **30**, e1802152 (2018).
52. J. Li *et al*., *Sci. Adv.* **8**, eabj9756 (2022).

ACKNOWLEDGMENTS

Funding: This work was supported by the National Natural Science Foundation of China (grants 62134009 and 62121005 to W.L.), the US Department of Energy (grant DE-FG02-07ER46426 to S.F.), and a Vannevar Bush Faculty Fellowship (to A.A.). **Author contributions:** Conceptualization: W.L., S.F., A.A., F.X.; Funding acquisition: W.L., S.F., A.A., D.L.; Investigation: F.X., W.J., J.R., H.P., N.Y., Y.A., L.L., X.K., Y.X., A.A., S.F., W.L.; Methodology: F.X., W.J., J.R., H.P., N.Y., Z.Z., K.J., S.T., T.L., X.S., L.L., D.L., Y.X., A.A., S.F., W.L.; Project administration: W.L.; Supervision: W.L., S.F., A.A.; Visualization: F.X., J.W., F.Z., S.F., W.L.; Writing – original draft: W.L., S.F., F.X.; Writing – review & editing: W.L., S.F., A.A., F.X., W.J., J.N., Y.X. **Competing interests:** Three patents (CN116774331A, CN116774332A, and CN116774333A) have been granted related to this work by W.L., F.X., H.P., N.Y., L.L., and Y.A. The remaining authors declare no competing interests. **Data and materials availability:** All data are available in the main text or the supplementary materials. Information requests should be directed to the corresponding authors.

SUPPLEMENTARY MATERIALS

science.org/doi/10.1126/science.adn2524
Materials and Methods
Supplementary Text
Figs. S1 to S23
Table S1
References (*53*–*83*)

Submitted 12 December 2023; resubmitted 18 May 2024
Accepted 10 October 2024
10.1126/science.adn2524